TU Delft

Delft University of Technology

Document Version
Final published version

Licence
CC BY

Citation (APA)
Ali, N., Zaid, O., Gebremariam, A. T., Chand, A., & Tariq, A. (2026). Thermal behavior of a concrete recycling unit during the transition from diesel-fired to electric hot air generator. *Case Studies in Thermal Engineering*, *79*, Article 107741. https://doi.org/10.1016/j.csite.2026.107741

Important note
To cite this publication, please use the final published version (if applicable).
Please check the document version above.

Copyright
In case the licence states “Dutch Copyright Act (Article 25fa)”, this publication was made available Green Open Access via the TU Delft Institutional Repository pursuant to Dutch Copyright Act (Article 25fa, the Taverne amendment). This provision does not affect copyright ownership.
Unless copyright is transferred by contract or statute, it remains with the copyright holder.

Sharing and reuse
Other than for strictly personal use, it is not permitted to download, forward or distribute the text or part of it, without the consent of the author(s) and/or copyright holder(s), unless the work is under an open content license such as Creative Commons.

Takedown policy
Please contact us and provide details if you believe this document breaches copyrights.
We will remove access to the work immediately and investigate your claim.

This work is downloaded from Delft University of Technology.

Case Studies in Thermal Engineering 79 (2026) 107741

Contents lists available at ScienceDirect

Case Studies in Thermal Engineering

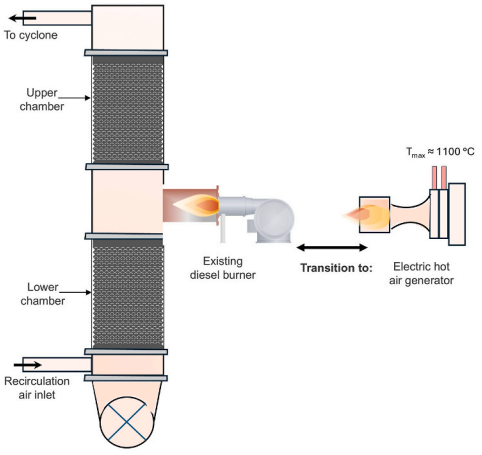
journal homepage: www.elsevier.com/locate/csite

Thermal behavior of a concrete recycling unit during the transition from diesel-fired to electric hot air generator

Nishab Ali [a,*], Osama Zaid [a], Abraham Teklay Gebremariam [a], Arun Chand [b], Andallib Tariq [b]

[a] Faculty of Civil Engineering and Geosciences, Resource and Recycling, Delft University of Technology, Delft, 2628, CN, the Netherlands
[b] AVTAR (Aerodynamics Visualization and Thermal Analysis Research) Lab, Mechanical and Industrial Engineering Department, Indian Institute of Technology Roorkee, Roorkee, 247667, India

GRAPHICAL ABSTRACT



ARTICLE INFO

Keywords:
Thermal performance
Industrial electrification
Decarbonization

ABSTRACT

For the advancement of sustainable and cleaner operation in concrete recycling, the Heating Air Classification System (HAS) requires replacing the existing diesel-fired burner with an electric heating technology. This study contributes to that transition by evaluating the suitability of electric hot air generators for HAS operational thermal needs. Through detailed numerical

* Corresponding author.
E-mail address: N.Ali@tudelft.nl (N. Ali).

https://doi.org/10.1016/j.csite.2026.107741
Received 13 November 2025; Received in revised form 10 January 2026; Accepted 23 January 2026
Available online 23 January 2026
2214-157X/© 2026 The Authors. Published by Elsevier Ltd. This is an open access article under the CC BY license (http://creativecommons.org/licenses/by/4.0/).

Energy Transition
Resources Recycling

analysis, the thermal performance and flow behavior of HAS are assessed across single (Cases: A1–A4) and dual inlet (Cases: B1–B4) configurations, and for a range of hot air inlet temperatures (800–950 °C). Spatial distributions of normalized temperature, velocity, and turbulent kinetic energy (*TKE*) are examined on multiple planes to characterize flow behavior, heating uniformity, and mixing. The results show that an electric hot air generator can nearly match the mean bulk temperature ($\langle T/T_0 \rangle \approx 0.49–0.50$) achieved with diesel systems, while providing notable improvements in thermal uniformity. Among all studied scenarios, the dual inlet configuration with lower hot air injection temperature (B1) achieves the lowest standard deviation (*0.080*) and coefficient of variation (*0.162*), ensuring the most consistent heating and minimal thermal gradients. These findings highlight that an electric hot air generator can be seen as one of the promising electrification pathways for HAS, supporting enhanced energy efficiency and cleaner production in concrete recycling applications.

Nomenclature			
C_{pw}	specific heat of water (kJ/kg·°C)	T_{so}	output temperature of solids
C_{ps}	specific heat of solids (kJ/kg·°C)	T_{st_o}	output temperature of steam
C_{pst}	specific heat of steam (kJ/kg·°c)	T_o	Reference injection temp. (Case A1), 800 °C
d	particle diameter (*mm*)	$\boldsymbol{u_i}$, $\boldsymbol{u_j}$, $\boldsymbol{u_k}$,	velocity vectors
ΔH_v	latent heat of vaporization (kJ/kg)	V_0	Reference inlet velocity of hot air (Case A1), 34 m/s
M	capacity of HAS (kg/hr)	*Greek symbols*	
$\dot{m}$	total air mass flow rate (kg/s)	ε	dissipation rate of turbulence (m^2/s^3)
$\dot{m}_h$	hot-air mass flow rate (kg/s)	ρ	density (kg/m^3)
$\dot{m}_r$	recirculated-air mass flow rate (kg/s)	μ	dynamic viscosity (Pa·s)
$\dot{m}_w$	mass of water	μ_t	turbulent viscosity (Pa·s)
N	number of sampled points	ν	kinematic viscosity (m^2/s)
Q_{duty}	total heat load required (kJ or kw)	τ	shear stress tensor (pa)
Q_{loss}	heat loss (kJ)	θ	temperature (°C or K)
q_w	energy required to raise the temperature of water	σ	standard deviation
q_v	energy required for vaporization	η	empirical constant or viscosity ratio
q_{st}	energy required to carry steam	*Abbreviations*	
q_s	energy required to heat solids	*ADR*	Advanced Dry Recovery
q_w	energy required to heat recirculated air	*CDW*	Construction and demolition waste
T_{ai}	aggregate inlet temperature (°C)	*CV*	Coefficient of Variation
T_{out}	outlet temperature, above cascade (°C)	*FRA*	Fine Recycled Aggregate
T_{ir}	recirculated-air inlet temperature (°C)	*HAS*	Heating Air Classification System
T_{ih}	hot-air inlet temperature (°C)	*RCP*	Recycled Cement-rich Powder
		TKE, k	Turbulent Kinetic Energy

1. Introduction

The increasing demand for concrete in the construction of residential houses, road infrastructure, corporate buildings, and other civil works is driving up the need for natural raw materials and energy. It is a significant contributor to CO_2 emissions, leading to environmental degradation, and plays a substantial role in the economies of nations that import these raw materials [1]. Furthermore, at the end of the concrete lifecycle, demolition waste again poses an environmental challenge to land allocation for its proper disposal [2]. Construction and demolition waste (*CDW*) is one of the largest waste streams generated. Therefore, to mitigate the serious concern of environmental degradation, the depletion of natural resources requires adopting circularity and sustainability in the concrete production and consumption industry.

One of the best measures to implement circularity in the concrete industry is to apply recycling practices, *i.e.,* recycling the end-of-life (EoL) concrete waste. Due to the large volume and high potential of CDW recycling/reusing, it is found to be a promising waste stream by the European Commission [3,4]. Recycling CDW, particularly concrete, offers a sustainable solution by reducing the need for virgin materials, minimizing waste, and decarbonization its lifecycle.

The existing recycling of CDW includes crushing to obtain secondary aggregates, the major proportion (i.e., only 95 %) of which is typically employed in low-grade applications [5–7] such as road civil works [8–10]. Only a small fraction (i.e., only 5 %) of recovered concrete waste is used as gravel in the production of high-quality concrete. The approach of reusing concrete for low-grade applications is not economically efficient due to the downcycling of higher-value materials [11].

Recent advancements in material engineering have emphasized the importance of maintaining material quality during recycling to enable effective reuse for high-performance applications, a strategy similar to those adopted in advanced composite and hybrid material systems [12–14]. Studies on polymer, metal-matrix, and fiber-reinforced composites demonstrate that controlled processing routes, reinforcement dispersion, and thermal treatment have a significant influence on mechanical integrity, durability, and functional performance. These findings highlight the importance of process-driven material refinement, which is directly relevant to concrete recycling technologies aiming for high-grade material recovery.

To preserve the resource value during recycling/reusing by obtaining high-grade reusable material from CDW waste, TU Delft recently developed two innovative technologies, i.e., Advanced Dry Recovery (ADR) and the Heated Air Classification System (HAS)

[15]. EoL concrete after passing through the jaw crusher is effectively segregated into the coarse (4–16 mm) and fine recycled aggregates, FRA (0–4 mm) by the ADR technology [15]. The FRA is further processed by the HAS to obtain high-value fine recycled aggregates (0.25–4 mm) and recycled cement-rich powder, RCP (0–0.25 mm). The recycled fine aggregates and RCP obtained from these innovative technologies can be effectively utilized in the production of new concrete [16,17].

The HAS system is engineered to expose fine aggregates to high-temperature airflow, enabling efficient drying and removal of contaminants such as wood and plastic found in Construction and Demolition Waste (C&DW). Operated as a fluidized-type reactor, the process relies on heated air for moisture evaporation and activation of ultrafine particles, mainly hydrated cement residues [15]. The current generation HAS employs a diesel-fired burner as its heat source, which brings significant drawbacks: elevated carbon emissions, environmental harm, and depletion of fossil resources. Moreover, direct flame contact with aggregates causes smoke residue buildup and uneven heating, thereby limiting their sustainable use in construction applications.

To overcome these environmental and quality challenges, a shift toward cleaner, more sustainable heating methods is essential in such high-carbon-emitting sectors [18–20]. Transitioning from diesel combustion to suitable electric heating technologies, such as hot air generators, resistive heating, induction heating, or plasma heating, offers a promising pathway. This study initiates the evaluation of suitable electric heating options for HAS. However, before implementing any of such solutions, it is necessary to rigorously assess their feasibility in meeting HAS's operational demands and to gain a detailed understanding of associated temperature and flow fields. Comprehensive aerothermal analyses are crucial for optimizing heat transfer, ensuring uniform heating, and improving the system's energy efficiency. Only the electric hot air generator technique has been selected for this initial investigation due to its operational similarity to the current setup, allowing straightforward retrofit with minimal structural alterations.

In summary, the objective of this novel work is to assess the feasibility of an electric hot air generator as a replacement for the existing diesel burner while meeting the thermal needs of HAS. Through systematic numerical simulations, the research explores a range of mixing ratios, injection temperatures, and both single and dual-inlet configurations, aiming to characterize HAS's aerothermal performance under electric heating. The results are presented as detailed temperature and velocity fields, time-averaged streamlines, and turbulence characteristics, which offer valuable insights into the flow and heat transfer processes within HAS. These findings provide a scientific foundation for the optimization and future development of efficient, electrified heating systems for concrete recycling. Ultimately, this work supports a broader transition toward low-carbon, resource-efficient thermal technologies in industrial operation, with potential applicability to other high-temperature industrial applications.

2. Methodology and description of HAS

2.1. Working principle and geometry

The HAS system is designed to expose fine aggregates to high-temperature airflow; the thermal energy causes moisture removal by evaporation and activates ultrafine particles. It features a series of curved cascades embedded within its vertical structure, arranged in

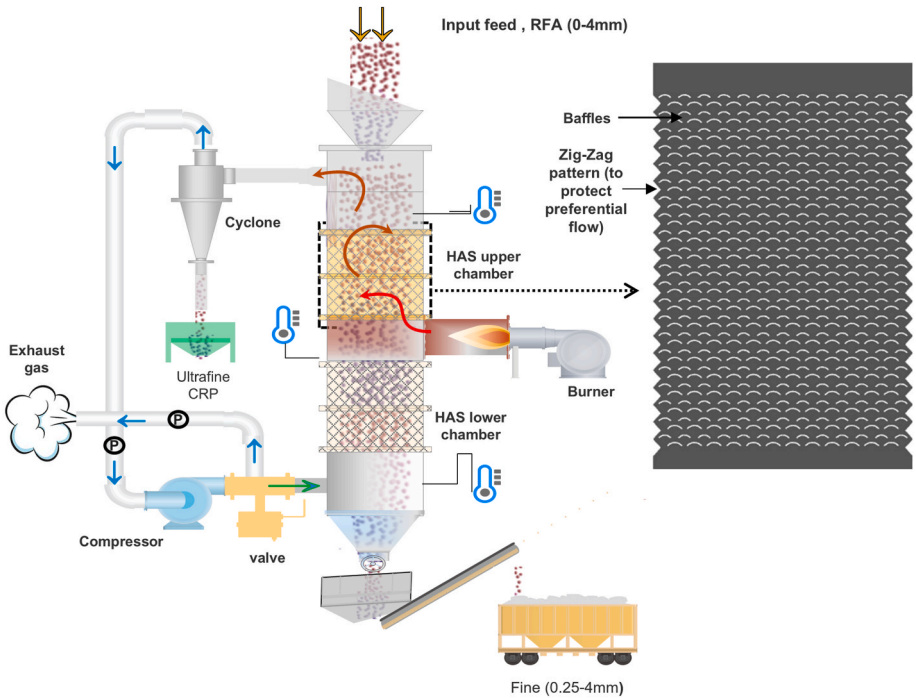


Fig. 1. Schematic of Heating Air classification System (HAS), also showing the upper chamber.

both the upper and lower sections, as illustrated in Fig. 1. The upper cascades increase the residence time of particles, hence enhancing heat transfer by maximizing contact between aggregates and hot air. As aggregates move from one cascade to another, they undergo better thermal exposure and fragmentation, improving the efficiency of the process. Dried, activated, ultrafine particles are dragged upward by the airflow towards the cyclone, while heavier particles settle into a collection bin as they pass through the lower cascade region.

A compressor facilitates airflow circulation required for the operation of the HAS. The lighter particles carried away by the air are pushed into the cyclone separator, which separates the ultrafine particles from the airstream, while directing warm air back into the recirculation system. The lower cascades assist in recovering thermal energy from the high-temperature solid back to recirculating moist air, thereby reducing thermal energy requirements and improving cycle efficiency.

The cascades are composed of curved baffles with convex sides arranged in a staggered fashion in rows, as shown in Fig. 2. To prevent preferential air/aggregates flow within the HAS, the side wall of the cascade chamber features a zigzag pattern. The present work is particularly focused on characterizing the aero-thermal behavior in the upper cascade and burner region with an electric hot air injection, where the actual process of aggregate separation takes place.

2.2. Energy and airflow requirement

The current HAS system at TU Delft has a processing capacity of 1 ton per hour. The fine fraction is often moist; therefore, an average moisture content of 10 % is assumed for RFAs. The theoretical energy requirement for processing this aggregate can be calculated by using Equation (1).

$$Q_{duty} = \left[m_w C_{pw} \Delta Tw\right] + \left[m(\Delta X)\Delta H_v\right] + \left[m_{steam} C_{Pst} \Delta Tst\right] + \left[m_{steam} Cp_s \Delta Ts\right] + \left[Q_{loss}\right] \quad (1)$$

Based on the realistic assumptions/measurements given in Table 1. The following requirement of heat energy has been estimated:
Energy required to raise the temperature of water to boiling temperature, $q_w = 36836.8$ kJ,
Energy required for vaporization, $q_v = 226000$ kJ,
Energy required to carry steam, $q_{st} = 26000$ kJ,
Energy required to heat solids, $q_s = 124200$ kJ,
Energy required to heat incoming air, $q_a = 75000$ kJ.
$Q_{duty} = q_w + q_v + q_{st+}q_s + q_{a+}Q_{loss}$ (assuming 10–12 % of total)
$Q_{duty} \approx 546600$ kJ *or* $\sim$ 150 kW.

To obtain temperature information within the actual HAS during operation, a K-type thermocouple has been installed at various locations within the HAS, as shown in Fig. 6. The temperature information is used as feedback to control the feed of aggregates into the system.

3. Numerical details

As mentioned above, the existing HAS uses a diesel-based burner, which exhibits different thermal behavior compared to electric

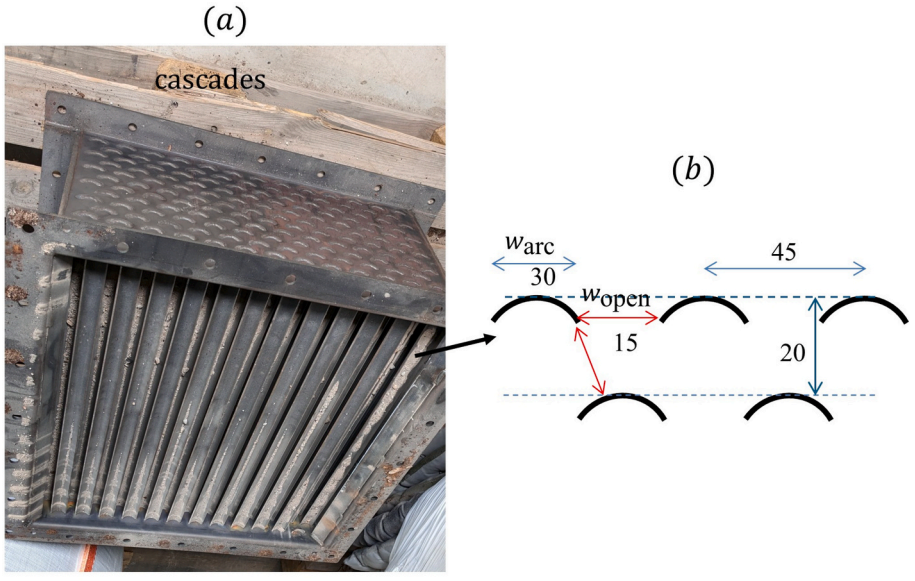


Fig. 2. (a) Actual view of cascade, (b) dimensions (mm) of curved baffles, not to scale.

Table 1
HAS realistic assumptions/measurement.

Description	Value
capacity of HAS (M)	1000 kg/h
moisture fraction (ΔX)	10 %
mass of water (m_w)	100 kg
heat capacity of water (C_{pw})	4.186
heat capacity of solid (C_{ps})	~1 kJ/kg ^oC
heat capacity of steam (C_{Pst})	2 kJ/kg ^oC
heat of vaporization (ΔH_v)	2260 kJ/kg
aggregate input temperature (T_{ai})	~ 12 ^oC
output temperature of solids (T_{so})	~ 150 ^oC
Max. temperature of steam (T_{st_o})	~ 230 ^oC
$\Delta T_w \approx (T_{boiling} - T_{ai})$	~ 88 ^oC
$\Delta T_{st} \approx (T_{st_o} - T_{boiling})$	~ 130 ^oC
$\Delta T_s \approx (T_{so} - T_{ai})$	~ 138 ^oC

heating technology. The flame produced by the burner has entirely different inherent spatial thermal and turbulence characteristics. However, the hot air generator produces a blast of hot air (non-reactive), therefore, prior to proceeding with the transition into the existing HAS system, it requires a detailed understanding of the flow and temperature distribution.

Consequently, a detailed numerical investigation has been conducted using hot air injections with varying mixing ratios, injection temperatures, and injection configurations. For a more realistic approach, the study was performed using the same dimensional geometry as the actual HAS dimension. The burner is supposed to be replaced by a hot air flow, which is assumed to come from an electric hot air generator, as shown in Fig. 3. Since the computational domain features a series of curved staggered cascades, creating a complex geometry, polyhedral meshes are generated. Comparatively finer meshes have been generated in the near-wall region, especially near the curved cascades, as illustrated in Fig. 4.

Summarizing, this study simulated eight CFD cases to evaluate the effect of hot air inlet configuration and mixing ratio on the aerothermal performance of the HAS, as shown in Table 2. The two configurations considered are Case A, with a single hot air inlet, and

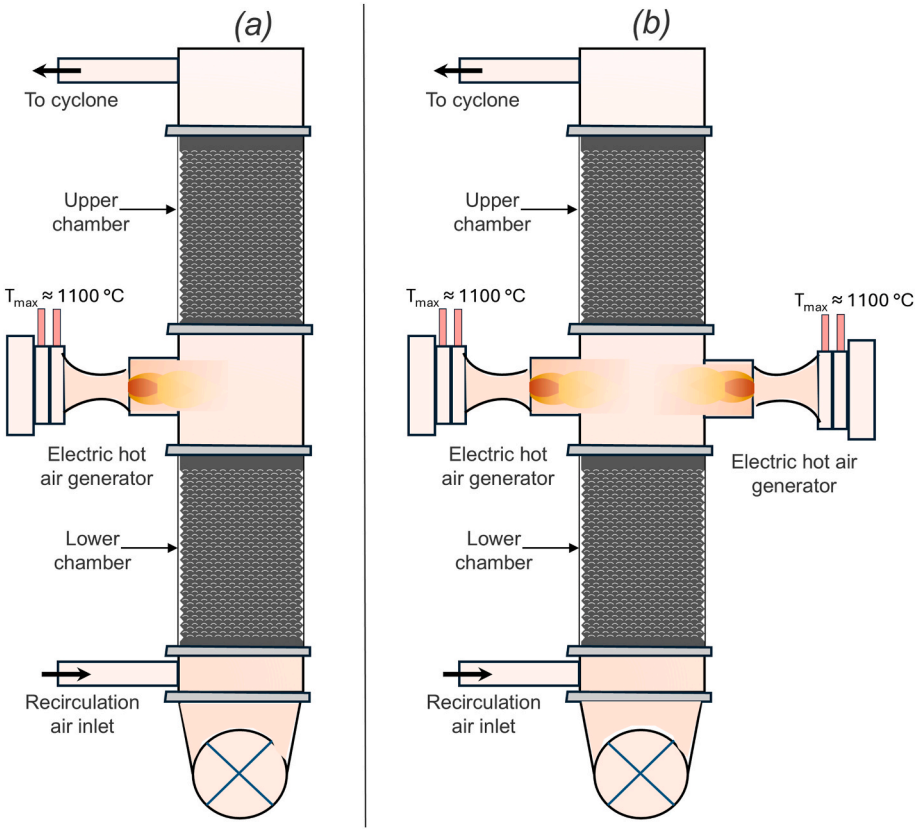


Fig. 3. Sketch showing the replacement of the burner with an electric hot air generator; (a) studied case A, i.e., single hot air injection, (b) studied case B, i.e., dual hot air injection.

Case B, with dual hot air inlets, as shown in the above Fig. 3a & b. It becomes a kind of T-junction near the hot air injection, in which fluid streams at different temperatures mix [21–23]. Each configuration was analyzed with four different hot air inlet temperatures: 800 °C, 850 °C, 900 °C, and 950 °C. These temperatures were selected based on realistic performance ranges of commercially available electric hot air generators (*Kanthal Flow heaters*) that could supply the thermal energy required for HAS operations.

To drag the ultra-fine ($d \leq 0.2$ mm) upward into the cyclone, the system requires a specified range of velocity above the cascade region, which should be higher than the terminal velocity of particles, *i.e.,* 2–3 m/s at a temperature of $T_{out} \approx 150$–200 °C (in the upper region of HAS). Therefore, accordingly, the total mass flow rate ($\dot{m}$) from recirculation and the hot air side should be ≈ 0.65 kg/s. The velocity within the HAS is determined by the temperature variation (due to density changes) in this region. The temperature distribution across the HAS is further dependent upon the mixing ratio and injection temperature.

While the total mass flow injection remains constant at $\dot{m} \sim 0.65$ kg/s, as the injection temperature of hot air varies (800–950 °C), the mass flow of hot ($\dot{m}_h$) and recirculation air ($\dot{m}r = \dot{m} - \dot{m}_h$) set accordingly to deliver the required thermal energy (~150 kW) to the system. It is essential to note that for Cases A, the hot air injection from a single hot air generator is equal to $\dot{m}_h$, whereas for Cases B, it is equal to $\dot{m}_h/2 + \dot{m}_h/2$ from each side, *i.e,* a total of $\dot{m}_h$ from both sides.

3.1. Turbulence model

The realizable k-ε turbulence model (which is a type of Reynolds-Averaged Navier-Stokes, RANS model) with enhanced wall treatment in *ANSYS FLUENT 2024R2* is selected for the present work. This model is typically used in similar engineering applications due to its balance between accuracy and computational efficiency [24]. However, the Reynolds-Averaged Navier-Stokes (RANS) models, such as realizable k-ε, may not capture flow dynamics as precisely as Direct Numerical Simulation (DNS) or Large Eddy Simulation (LES), but these can offer a practical approach by accurately predicting the mean flow field with significantly lower computational cost [25].

To ensure the reliability of the selected turbulence model, a comparative assessment was performed between the realizable k-ε and the Shear Stress Transport (SST) k-ω model. The realizable k-ε model demonstrated acceptable agreement with the temperature

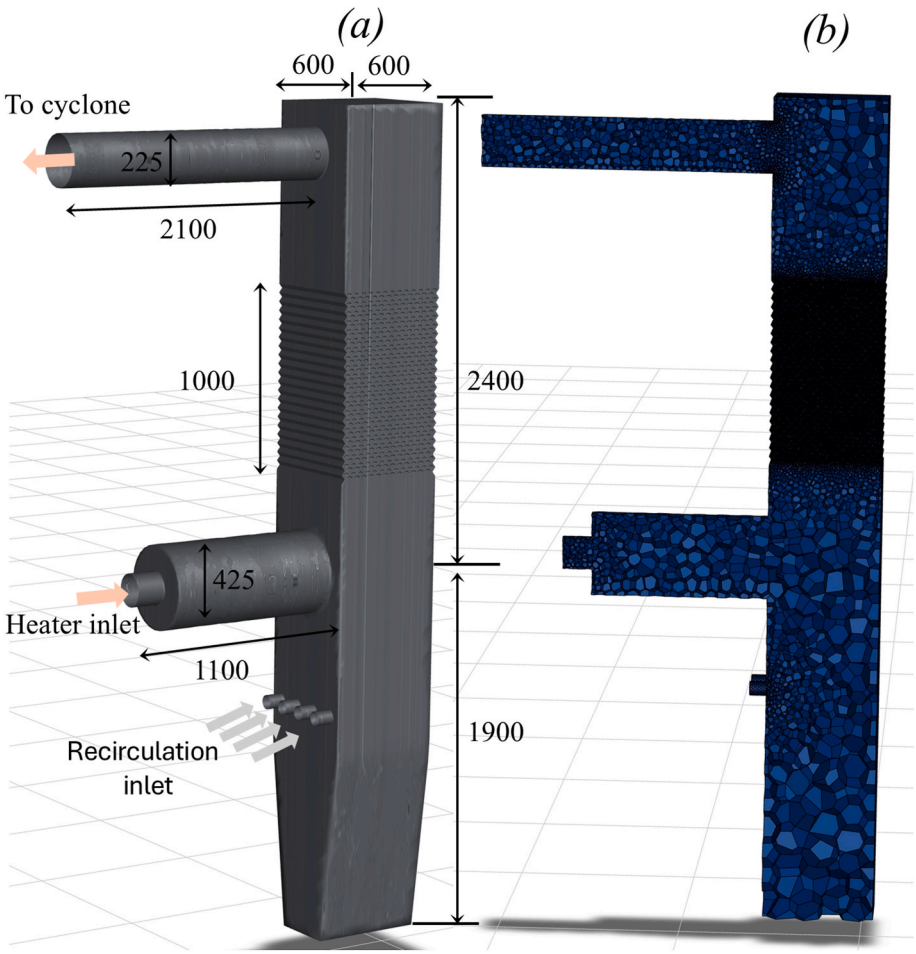


Fig. 4. (a) Dimensions (*mm*) of computational geometry, and (b) computational grid for single injection arrangement.

Table 2
The following table summarizes the simulation conditions for each case.

Case	Hot Air Inlet Temp, T_{ih} (°C)	Recirc. Air Inlet Temp, T_{ir} (°C)	Mass Flow Rate (Hot Air, $\dot{m}_h$) [kg/s]	Mass Flow Rate (Recirc. Air $\dot{m}_r$) [kg/s]
A1	800	125	0.26	0.39
A2	850	125	0.24	0.41
A3	900	125	0.22	0.43
A4	950	125	0.20	0.45
B1	800	125	0.26	0.39
B2	850	125	0.24	0.41
B3	900	125	0.22	0.43
B4	950	125	0.20	0.45

distribution obtained from experiments, while also being computationally more efficient than the SST k-ω model. Steady-state numerical simulations are conducted to obtain a time-invariant mean flow field. The governing RANS equations, along with the energy equation used in this study, are presented below [26,27].

$$\text{Continuity equation}: \frac{\partial}{\partial x_i}(\rho u_i) = 0 \tag{2}$$

Momentum equation:

$$\frac{\partial}{\partial x_j}(\rho u_i u_j) = -\frac{\partial p}{\partial x_i} + \frac{\partial}{\partial x_j}\left[\mu\left(\frac{\partial u_i}{\partial x_j} + \frac{\partial u_j}{\partial x_i} - \frac{2}{3}\delta_{ij}\frac{\partial u_k}{\partial x_k}\right)\right] + \frac{\partial}{\partial x_j}\left(-\rho\overline{u_i' u_j'}\right) \tag{3}$$

$$\text{Energy equation}: \frac{\partial}{\partial x_i}(\rho u_i T) = \frac{\partial}{\partial x_j}\left[\left(\frac{\mu}{Pr} + \frac{\mu_t}{Pr_t}\right)\frac{\partial T}{\partial x_j} + u_i\left(\tau_{ij}\right)_{eff}\right] \tag{4}$$

$$\text{where, } \left(-\rho\overline{u_i' u_j'}\right) = \mu_t\left(\frac{\partial u_i}{\partial x_j} + \frac{\partial u_j}{\partial x_i}\right) - \frac{2}{3}\left(\rho k + \mu_t\frac{\partial u_k}{\partial x_k}\right)\delta_{ij}, \text{ and} \tag{5}$$

$$\left(\tau_{ij}\right)_{eff} = \mu_{eff}\left(\frac{\partial u_i}{\partial x_j} + \frac{\partial u_j}{\partial x_i}\right) - \frac{2}{3}\left(\mu_{eff}\frac{\partial u_k}{\partial x_k}\right)\delta_{ij} \tag{6}$$

The equation for turbulent kinetic energy (k) and the dissipation rate of turbulence (ε) in the realizable $k-\varepsilon$ turbulence model are given as follows:

$$\frac{\partial}{\partial x_i}.(\rho k u_i) = \frac{\partial}{\partial x_i}.\left[\left(\mu + \frac{\mu_t}{\sigma_k}\right)\frac{\partial k}{\partial x_i}\right] + G_k - \rho\varepsilon - Y_M + S_k \tag{7}$$

$$\frac{\partial}{\partial x_i}.(\rho\varepsilon u_i) = \frac{\partial}{\partial x_i}.\left[\left(\mu + \frac{\mu_t}{\sigma_\varepsilon}\right)\frac{\partial \varepsilon}{\partial x_i}\right] + \rho C_1 S_\varepsilon - \rho C_2\frac{\varepsilon^2}{k + \sqrt{\nu\varepsilon}} + C_{1\varepsilon}\frac{\varepsilon}{k}C_{3\varepsilon}G_b + S_\varepsilon \tag{8}$$

where constants: $C_1 = \max\left[0.43, \frac{\eta}{\eta+5}\right], \eta = S\frac{k}{\varepsilon}, S = \sqrt{2S_{ij}S_{ij}}$, $C_{1\varepsilon} = 1.44$, $C_2 = 1.9$,

$\sigma_k = 1, \sigma_\varepsilon = 1.2$

3.2. Assumptions & numerical methodology

The following assumptions are considered for the numerical analysis:

a. The air is used as the working fluid, assumed incompressible, with constant thermophysical properties, and exists in a single phase, without water vapors and aggregates.
b. The flow is fully turbulent, and steady-state conditions prevail within the computational domain.
c. All the walls are assumed to be smooth.

The simulations are performed using the ANSYS FLUENT 2024 R2, which is based on the finite volume method (FVM). For pressure-velocity coupling, the SIMPLEC (Semi-Implicit Method for Pressure-Linked Equations-Consistent) algorithm is employed. The Green-Gauss node-based discretization is used for gradient calculations, while a second-order interpolation scheme is applied for pressure. The governing equations are spatially discretized using a second-order upwind scheme to enhance numerical accuracy. To ensure solution convergence, residual errors are monitored for key governing equations, with convergence criteria set as follows: Continuity equation; 1×10^{-4}, Momentum equation; 1×10^{-6}, and Energy equation; 1×10^{-8}.

Additionally, the momentum (1×10^{-6}) and energy (1×10^{-8}) convergence criteria are consistently satisfied throughout the simulations. To further ensure steady-state conditions, the surface-averaged temperature and velocity at the x-y plane located near hot

air injection (*Z2,* $z/D_h = 3.25$*)* are continuously monitored. A convergence test is conducted for Case A1, using two different criteria (10^{-4} and 10^{-5}). The velocity distribution at the centerline of plane Z2 (*x-y* plane) is compared for both cases. The outcomes demonstrated very good agreement between velocity profiles, with a maximum uncertainty of only 0.06 %. However, the time required for residuals to drop below 10^{-5} was found to be almost 1.8 times that for 10^{-4}, making 1×10^{-4} the optimal choice based on computational efficiency and accuracy.

3.3. Boundary conditions

The recirculation air coming from the four inlets is assumed to be incompressible with constant thermophysical properties at 125°C, for all cases. While the hot air is injected at different temperatures in various cases (800 °C, 850 °C, 900 °C, and 950 °C) from both single and dual injection configurations, the details are provided in Table 2. The total incoming mass flow from the heater and recirculation sides remains constant ($\dot{m} \sim 0.65$ kg/s); however, the ratio between these is varied as per injection temperature T_{ih}, see Table 2. Consequently, a constant mass inflow boundary and temperature condition is applied for each case, as given in Table 2. At the outlet, an outflow boundary condition is imposed, ensuring a zero normal gradient for all variables except pressure. All walls adhere to no-slip, no-penetration and adiabatic conditions.

3.4. Grid independence

A high-quality, structured mesh was generated using ANSYS meshing for the geometry. The mesh consists of polyhedral elements with refined resolution near the wall region to accurately resolve flow separation and thermal gradients. Special attention was given to wall-adjacent cells to maintain a dimensionless wall distance ($y^+ < 1$) for reliable near-wall turbulence modeling. To ensure mesh-independent results, a grid sensitivity study was conducted using three mesh densities: coarse (~4.2 million cells), medium (~7.5 million cells), and fine (~11.6 million cells)

The assessment was conducted for constant mass flow rate ($\dot{m}_h = 0.1$ *and* $\dot{m}_r = 0.55$*, i.e.,* $\dot{m} = 0.65$) with all other conditions remaining the same for all mesh densities. The normalized velocity (V/V_0) and temperature (T/T_0) profiles along the *y*-direction (y/D_h) at the central axial location ($x/D_h = 0$) of the *x-y* plane located near the hot air injection (Z2, $z/D_h = 3.25$), the location are illustrated later in Fig. 6a. Here, in the upcoming results, the temperature and velocity distribution have been normalized by the mean hot entry temperature and velocity for Case A1, i.e., T_0 (800 $_0$C) and V_0 (34 m/s).

As shown in Fig. 5, the velocity profile obtained from the coarse mesh deviates slightly from those of the medium and fine meshes, particularly near the wall regions, indicating an under-resolution of boundary layer structures. However, the medium and fine mesh profiles show close agreement across the entire span, with a maximum deviation of less than 2 % in peak velocity values. Similarly, the temperature distribution exhibits notable differences for the coarse grid, especially in regions of thermal gradient near the walls. The medium and fine meshes demonstrate a consistent profile with a maximum variation of less than 1.5 %, confirming sufficient resolution of thermal fields. Based on this analysis, the medium mesh (~7.5 million cells) was chosen for all subsequent simulations, as it offers a reliable balance between computational cost and solution accuracy.

3.5. Model validation

To validate the numerical model developed for the HAS setup, temperature predictions from simulations (Case A1) were compared against experimental measurements at six distinct vertical locations along the *z*-axis of the main chamber. Measurement points (*k*-type thermocouple) were located at Z_1 ($z/D_h = 1.0$) near the bottom of the chamber, Z_2 ($z/D_h = 3.25$) near the hot air injection, Z_3 ($z/D_h = 4.1$) at the entry of the upper cascade, Z_4 ($z/D_h = 4.94$) at the center of the cascades, Z_5 ($z/D_h = 5.6$) close to the exit of the cascade, and

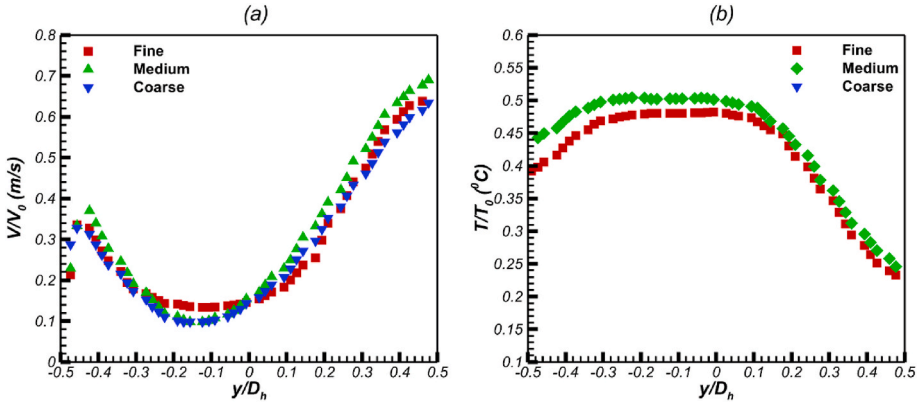


Fig. 5. (a) Velocity, and (b) temperature profiles at the central axial location ($x/D_h = 0$) of the *x-y* plane located near the hot air injection (Z2, $z/D_h = 3.25$).

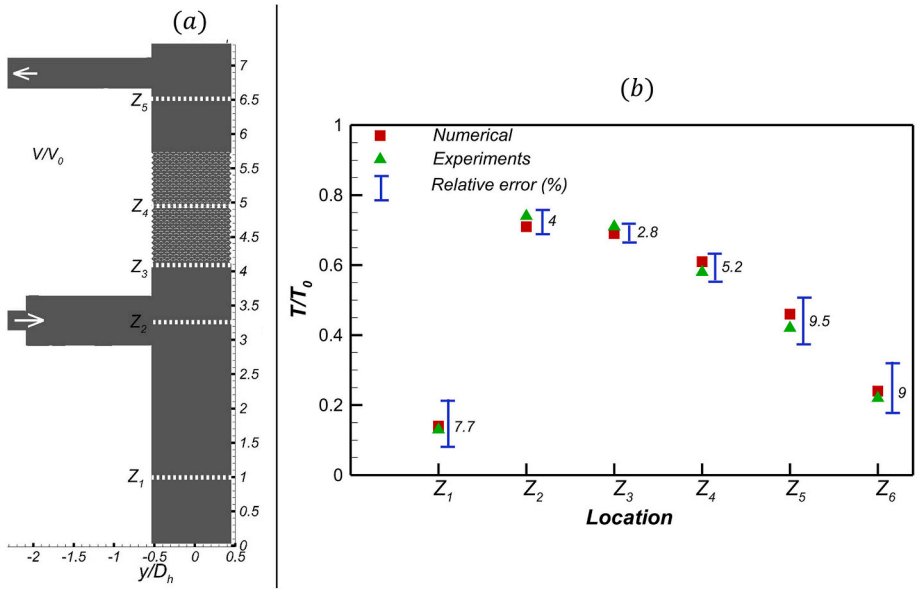


Fig. 6. (a) Thermocouple/planes (Z_1, Z_2, Z_3, Z_4, Z_5, and Z_6) locations, *(b)* Comparison of the temperature profile, experimental vs numerical, also showing the relative percentage error.

Z_6 ($z/D_h = 6.5$) near the outlet of the main chamber, as illustrated in Fig. 6a.

In the experiments, temperatures were recorded using thermocouples placed at the center along the x-axis and inserted 0.1 m into the *y*-direction. These values represent the time-averaged temperatures once the system reached a thermal steady state (after ~20 min of continuous operation without aggregate feeding). For the simulations, the temperature selected for validation is the centerline temperature along the *z*-direction at $x/D_h = 0$ and $y/D_h = 0$. The centerline temperature is selected for comparison because the simulated temperature field exhibits spatial non-uniformity in the transverse (*x*–*y*) plane due to inherent mixing differences between the diesel fire and hot gas from the electric generator. Therefore, the centerline location provides a representative and consistent reference point that best corresponds to the experimental thermocouple placement, enabling a meaningful comparison between experimental and numerical results.

Fig. 6b presents the comparison of normalized temperature (T/T_0) between experimental and numerical results. At Z_1, located at the bottom, the simulation shows slightly higher temperatures with a relative percentage error of ≈7.7, likely due to the absence of

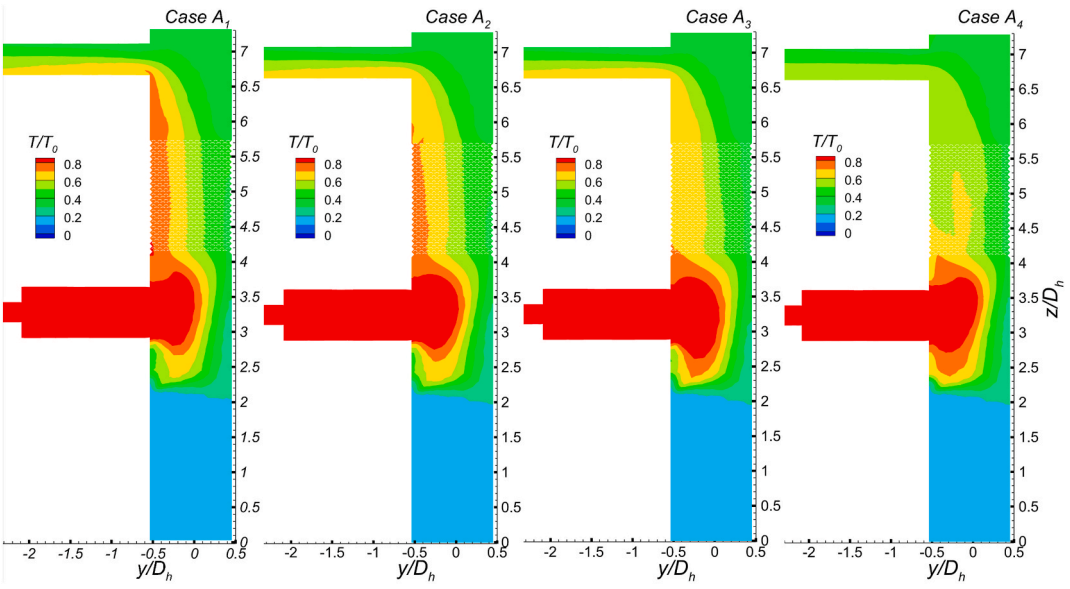


Fig. 7. Normalized temperature (T/T_0) distribution contours on the vertical *y* -*z* plane (located centrally at $x/D_h = 0$) for single hot injection, Case A.

wall heat losses in the numerical model, which are present in the real system. At Z_2, near the burner, the experimental temperatures are marginally higher (relative percentage error ≈ 4) owing to variable heat output from the burner over time, despite being at steady state, whereas the simulation applies a constant thermal inlet. At Z_3, near the cascade entry, experimental temperatures remain slightly elevated, possibly due to the cumulative heat effect in that region. For Z_4, Z_5, and Z_6 (the mid and exit regions of the cascade system), the numerical model predicts marginally higher temperatures compared to the experiments, with respective relative percentage errors of 5.2 %, 9.5 %, and 9 %. This trend is again attributed to the lack of heat loss to the surroundings in the computational model. Additionally, a slight discrepancy may also occur due to the comparison of average and point temperatures in the numerical and simulation cases, as discussed above. Overall, the comparison confirms that the numerical model reliably captures the thermal behavior of the HAS, with reasonable agreement across all locations, and highlights the influence of wall heat losses and burner fluctuations in the experimental setup.

4. Results and discussion

This section presents a comprehensive analysis of the aerothermal behavior within the HAS chamber under different inlet configurations and mixing scenarios. The numerical results are discussed in terms of temperature distribution, velocity fields, and turbulence characteristics, with a focus on understanding the thermal mixing and flow structure across the cascade region. Key insights are drawn to elucidate that if replacement of the burner with a hot air generator can successfully fulfill the thermal requirement of the HAS, and further support optimization of heater placement and flow design for electric heating integration.

4.1. Thermal field

Figs. 7 and 8 present the normalized temperature (T/T_0) distribution contours on the vertical y-z plane (located centrally at $x/D_h = 0$) for Case A (single hot air inlet) and Case B (dual hot air inlets), respectively, under four different inlet temperatures (800 °C, 850 °C, 900 °C, and 950 °C). These contours reveal distinct differences in temperature distribution, mixing efficiency, and thermal uniformity within the HAS chamber for the two configurations.

In Case A, the thermal plume from the single inlet shows a relatively asymmetric spread, with higher temperatures concentrated near the injection and along one side ($y/D_h < 0$). At lower inlet temperatures (Cases A1 and A2), the thermal gradient is significantly pronounced, and mixing between recirculated and heated air remains limited across the cascade region. As the hot air temperature increases to 900 °C and 950 °C (Cases A3 and A4), the thermal field penetrates slightly deeper into the cascade zone, and a better homogeneity is observed in the lateral direction. Rather than fully mixing with the hot air injection stream, a part of the recirculated air preferred its path towards the other side of the injection by pushing the heated air towards the injection side ($y/D_h \approx -0.5$ to -0.1). Thus, the bulk of the injected hot air stream concentrates along the injection side, while the flow is directed upward from the hot air entry region; consequently, a temperature non-uniformity remains apparent in the upper regions of the HAS.

In contrast, Case B with dual hot air inlets exhibits improved thermal uniformity across the cascade zone. For all temperature levels (Cases B1–B4), the high-temperature zone is more symmetrically distributed across the y-axis, and hot air effectively reaches the upper sections of the HAS ($z/D_h \approx 4.0$ to 5.0). For Cases B1 and B2, a near-uniform thermal field is established within the cascade core ($z/D_h = 4$ to 6), indicating enhanced convective mixing. It demonstrates the dual jet mixing improvement at lower injection temperatures, *i.e.,* high-velocity injection. A similar type of improved mixing with a higher blown ratio of jets is observed by Zhou & Hu [28]. The uniformity in these regions directly contributes to improved thermal exposure of fine aggregate particles.

Furthermore, at $z/D_h \approx 6$ above the cascades, Case B contours display smoother temperature gradients and fewer localized hot/cold zones than Case A, suggesting better mixing efficiency above the cascade as well. This is particularly beneficial for pre-heating and

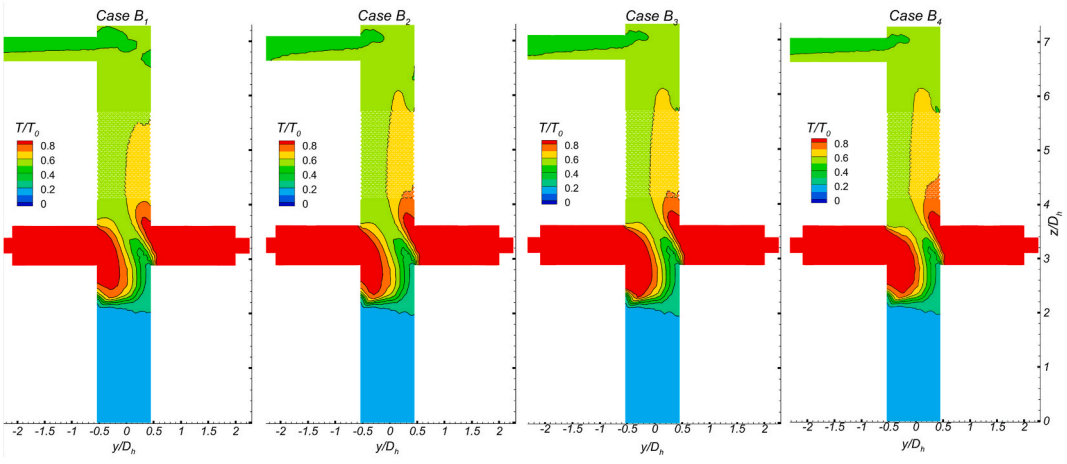


Fig. 8. Normalized temperature (T/T_0) distribution contours on the vertical y-z plane (located centrally at $x/D_h = 0$) for dual hot injection, Case B.

uniformly initiating moisture drying from aggregates above the upper chamber of HAS. Additionally, the peak temperature in Case A is shifted toward one side, while in Case B, it is comparatively more centralized, which may lead to more balanced particle heating and reduced risk of thermal hotspots.

For a detailed understanding of the temperature fields across the cross-sectional planes (*x-y* planes), the temperature contours were extracted at two representative planes and shown in Figs. 9 and 10. The two notable planes for cross-sectional temperature field representation are (a) Z_2, near the hot air injection, and (b) at the center of the upper cascade region Z_4, see the locations in the above Fig. 6a. The objective is to further understand and evaluate thermal uniformity, mixing performance, and energy utilization efficiency.

For configuration A, thermal fields at plane Z_2 demonstrate that increasing the inlet temperature slightly enhances the overall coverage of high-temperature zones (Fig. 9a). Particularly in Cases A3 and A4 (T_i = 900 °C and 950 °C), regions with $T/T_0 \geq 0.75$ expand more specifically in the lateral direction (*i.e., y*-direction), indicating a slightly better heat propagation at the inlet. However, lateral non-uniformities are visible from $y/D_h \approx 0$ *to 0.45* in all the cases, suggesting incomplete transverse mixing between hot and recirculated air, which is more pronounced at lower injection temperatures.

At the center of the cascade (plane Z_4), a more diffused and symmetric temperature field is evident (Fig. 9b). A comparatively hotter region with symmetry along the center ($x/D_h \approx 0$) is more pronounced in lower-temperature cases (A1 and A2) towards the hot air injection side. While in cases A_3 and A_4, the symmetry along the $x/D_h \approx 0$ disappeared, and hot spots were observed on the left side (near $x/D_h \approx -0.4$ and $y/D_h \approx -0.4$ for A3) and the right side (near $x/D_h \approx 0.4$ and $y/D_h \approx -0.4$ for A4) corners, respectively. Despite the local hot spots, the overall stratification at plane Z_4 is reduced, confirming improved mixing as the air ascends across the HAS chamber.

In contrast, the dual-inlet configuration B shows distinct behavior due to the presence of two opposing inlets, as shown in Fig. 10. At plane Z_2, lateral mixing is significantly enhanced. High-temperature zones ($T/T_0 \geq 0.75$) expand more uniformly as the interaction of dual jets creates improved thermal fields and minimizes cold spots, especially in B1 and B2. The non-uniformities and layering for the dual inlet configuration are seen in the lateral direction, i.e., particularly the center region across the *y*-direction from $y/D_h \approx -0.2$ *to 0.4*.

At plane Z_4, while the upper cascade exhibits improved temperature distribution over the hot injection plane, thermal layering/gradients almost disappear in all the cases (Fig. 10b). The local hotspot is not observed in configuration B, and comparatively more uniform temperature fields is seen, which ranges from $T/T_0 \approx 0.45$ to 0.55, compared to $T/T_0 \approx 0.35$ to 0.75 for configuration A, suggesting a better and homogeneous mixing compared to configuration A. Overall, from the temperature distribution perspective, configuration B with lower inlet temperatures (B1 and B2) offers superior thermal uniformity, reduced hot spots, and enhanced energy efficiency at both planes.

The observed thermal patterns result from the interaction of jet momentum, buoyancy, and geometric confinement. In the single-inlet case, a dominant jet suppresses transverse entrainment, maintaining lateral temperature gradients, whereas the dual-inlet configuration generates opposing shear layers that enhance turbulent mixing and thermal diffusion. Consequently, improved uniformity in the dual-inlet system arises from flow-driven mixing rather than increased thermal input. For further insight into the effect of this transition (from diesel-fired to high-temperature electric hot air generator) on HAS operation, the flow behavior has been discussed in the upcoming section.

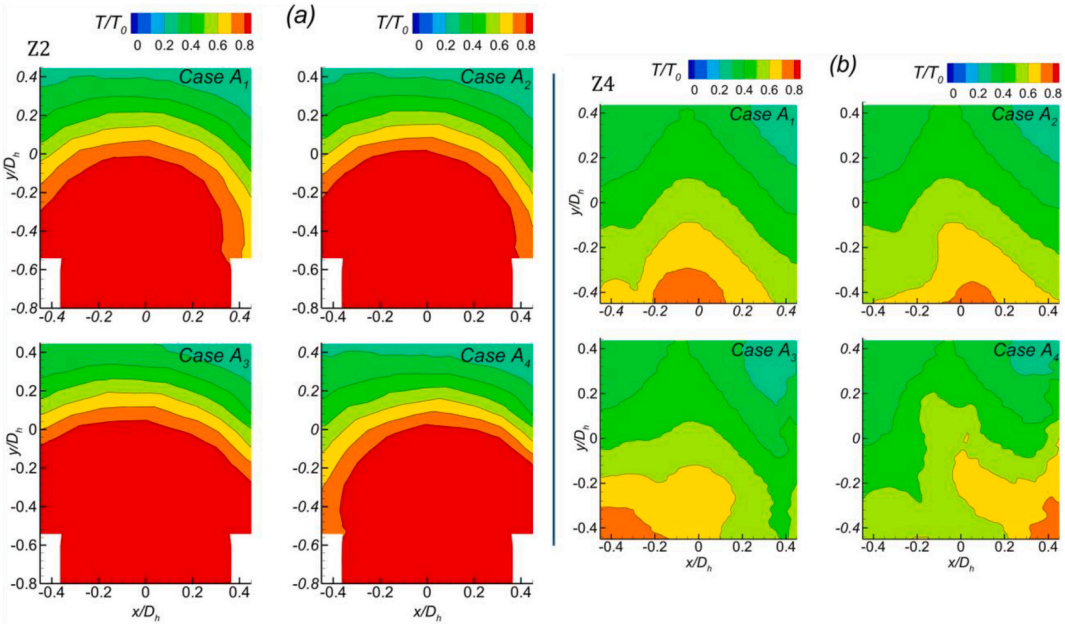


Fig. 9. Normalized temperature (T/T_0) distribution contours for single hot injection, Case A, (a) at Z_2, the *x* -*y* plane, (b) at Z_4, the *x* -*y* plane.

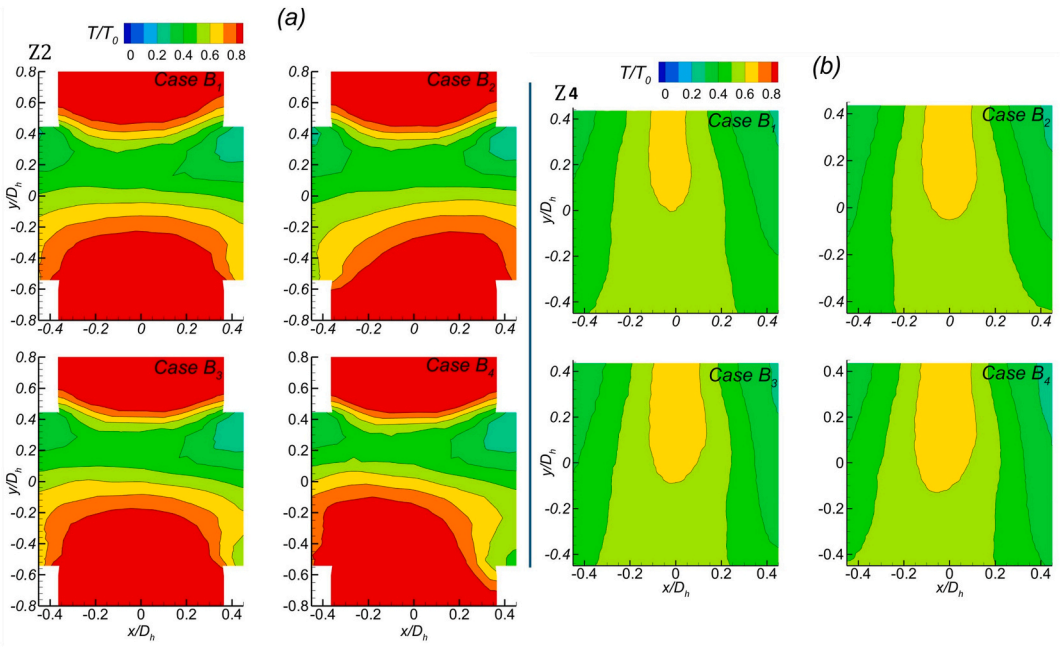


Fig. 10. Normalized temperature (T/T_0) distribution contours for dual hot injection, Case B, (a) at Z_2 the x -y plane, (b) at Z_4 the x -y plane.

4.2. Flow characteristics

The analysis of flow fields across both the y-z and x-y (horizontal at Z_2 injection plane) planes offers critical insight into the flow organization and its interaction with the observed thermal fields in the HAS chamber.

For the single inlet configurations (Cases A1–A4), the velocity maps in the y-z planes demonstrate the development of a large-scale recirculation zone near the recirculated air inlet (Fig. 11a). In all cases, a prominent ascending jet forms near the chamber's lower section with the highest normalized velocities ($V/V_0 \geq 0.2$) at the periphery of the vortex. The heated air at the entrance of the main chamber bifurcates, and a portion of it exhibits significant penetration towards the underside of the HAS chamber, extending up to $z/D_h \approx 2.3$. In a quest for a path required to flow, a part of the recirculated air pushes the heated air towards the injection side. Thus, the bulk of the heated air flow tends to concentrate along the injection side, resulting in heat concentration towards the injection side. Notably, for Case A4, the core velocity zone of hot air injection within the injection path slightly tilts upward, resisting the unsuitable penetration of hot air towards the bottom side of the chamber. For all cases, small-scale vortex structures are evident near the immediate upstream region towards the injection side, and at the top-most corner of the HAS chamber, which are marked by a white dotted circle. The first vortex leads to the entrapment/accumulation of heated air coming from the hot air injection side and, correspondingly, a high temperature spot is created (see Fig. 7). The second one entraps cool air at the top, farthest corner, and aligns with the lower temperature zone, undesirable for initial drying. Such entrainment of cold/hot air by the recirculation vortex, with reduced mixing, has also been noted by Ali et al. [29–32].

Examining these cases on the x-y plane at the injection plane (Z_2), the normalized velocity contours (Fig. 11b) further affirm a nearly centrally peaked symmetrical profile except case A4, the maximum velocities aligning along $x/D_h \approx 0$ for cases A1 to A3 and $x/D_h \approx 0.15$ for case A4. However, the high velocity zone in case A4 is offset, but the wider and stronger high velocity zone in this case leads the basis to penetrate the hot air towards the farther side of the cross section. It occurs during the ascent in the cascade zone, aiding the mixing and hence the reduced thermal gradients across the cascade for Case A4, as previously noted in temperature fields. Characteristically, the shadow of vortical zones develops near the interface of the injection pathways and the main chamber, as observed in the x-y plane, corresponding to local low-velocity (and high-temperature) pockets due to the accumulation/entrapment of hot air.

In contrast, the dual inlet configurations (Cases B_1–B_4) exhibit markedly different flow characteristics in both y-z and x-y planes, as shown in Fig. 12. The velocity fields depict two distinct, nearly symmetrical hot air jets entering from opposing sides in the lower region, which merge and interact. The interaction of two head-on hot air streams with an upward rising recirculated stream pushes the one hot air stream downward and the other upward. For configuration B, the dual inlet doesn't allow the cool, recirculated air to escape from the side of the chamber, unlike in configuration A. The streamlines reveal a counter-rotating structure near the injection, resulting in the accumulation of hot air in these regions. This pattern is slightly more pronounced at higher inlet temperatures, where the velocity and vortex coherency increase slightly, thereby restricting thermal coverage and enhancing stratification observed in the thermal fields for cases B3 and B4. Overall, the inherent symmetry of the dual inlets efficiently suppresses preferred flow and stagnant zones prevalent in the single inlet case, sustaining a homogeneous flow throughout the chamber's vertical extent, particularly at lower

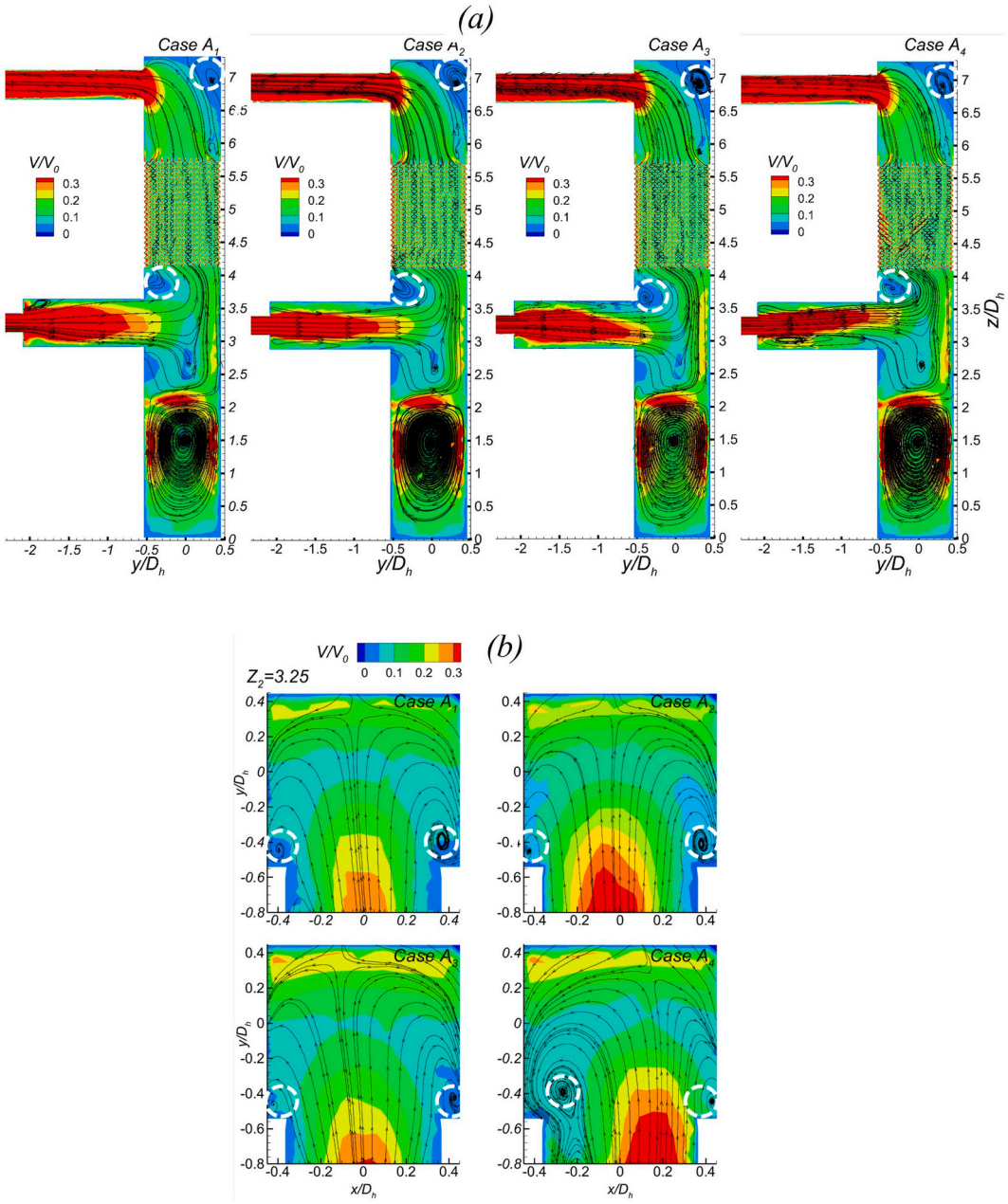


Fig. 11. Normalized velocity distribution (V/V_0) with time-averaged streamlines for single hot injection, Case A, (a) at the vertical *y-z* plane (located centrally at $x/D_h = 0$), (b) *x-y* plane, Z2.

Ti (cases B1 and B2).

On the horizontal Z_2 plane, the dual inlet arrangement (Cases B1–B4) maintains higher velocity inflow regions spanned across $y/D_h \approx 0.2$ to 0.4. Streamlines in these cases indicate rapid lateral spreading and a bifurcation near the mid-plane ($y/D_h \approx -0.2$ to 0), which sweeps low-velocity regions in these local areas. This bifurcation originates due to the head-on interaction of the dual heated air injection. As observed, increasing the inlet temperature does not show any significant change in flow behavior at this plane. In summary, the single inlet (Case A) produces a preferred flow, resulting in persistent asymmetries. The dual inlet (Case B) configuration, however, shows better symmetry, accelerates chamber-wide mixing, and minimizes regions of stagnant flow. Though the dual inlet arrangement exhibits an inherent better mixing and resistance to preferred flow, the injection temperature increment leads to slightly reduced lateral spread. For further strengthening the understanding of the mixing process, the discussion has been carried out in terms of turbulence characteristics in the upcoming section.

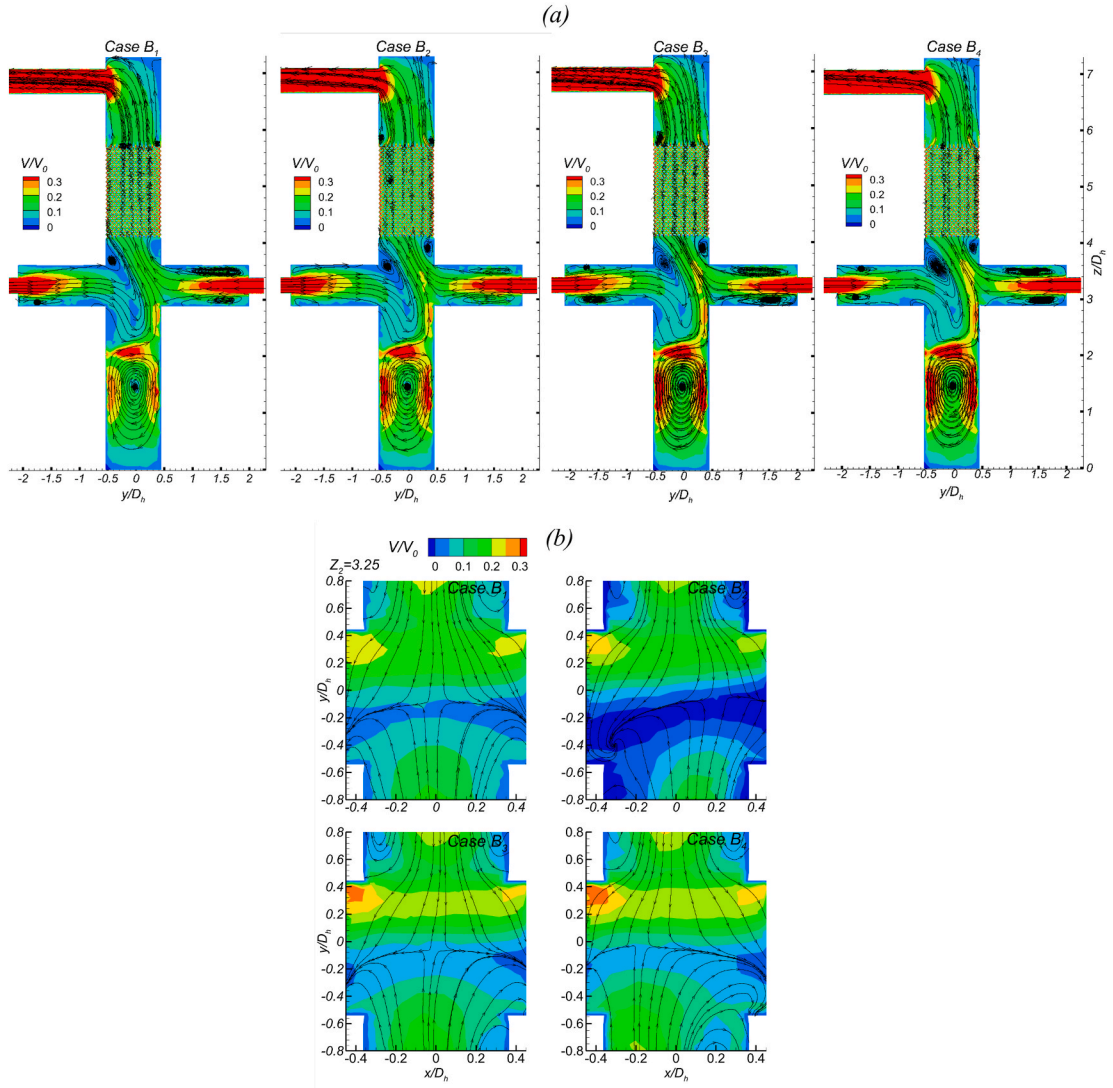


Fig. 12. Normalized velocity distribution (V/V_0) with time-averaged streamlines for dual hot injection, Case B, (a) at the vertical *y-z* plane (located centrally at $x/D_h = 0$), (b) *x-y* plane, Z2.

4.3. Turbulence analysis

The turbulent kinetic energy (TKE, denoted as *k*) distribution figures further support the understanding of the mixing performance and turbulence generation within the HAS chamber for both single (Case A) and dual inlet (Case B) configurations. When interpreted alongside the previously examined thermal and velocity fields, the TKE contours clarify the direct coupling between flow organization, turbulence, and resulting temperature uniformity throughout the HAS.

At the *y-z* plane, *k* distribution highlights that near the hot air entry region, turbulence is stronger for configuration A than for B, but its spread is comparatively more localized, as shown in Fig. 13a. It can be inferred that the localized mixing near the injection point is more significant; the injection side ($y/D_h \leq 0.2$) predominantly on the side toward which the ascending hot jet is deflected shows better mixing. It might be due to the high mass inflow rate through a single injection, leading to the evolution of high velocity gradients. This localized intensity of *k* for configuration A shows an enhancement at higher temperature injection but remains focused. The presence of cascades above the injection point strongly enhances the *k* and promotes significant local mixing in these regions. The *k* distribution substantiates prior observations from temperature and velocity field analyses, wherein the core upward flow, constrained to one side by geometric and buoyancy effects, creates spatially confined velocity and temperature fields.

On the *x-y* plane at the Z_2 injection point for Case A, the TKE is again concentrated near the hot stream core, with peak values at $x/D_h \approx 0$ and extending toward the primary outflow quadrant (see Fig. 13b). The presence of localized mixing "hotspots" aligns with the streamer-like structures seen in the velocity field, yet the peripheral regions remain relatively quiescent (low *k*), reaffirming that the single inlet, while capable of high local mixing, does not achieve system-wide turbulence necessary for optimal thermal uniformity.

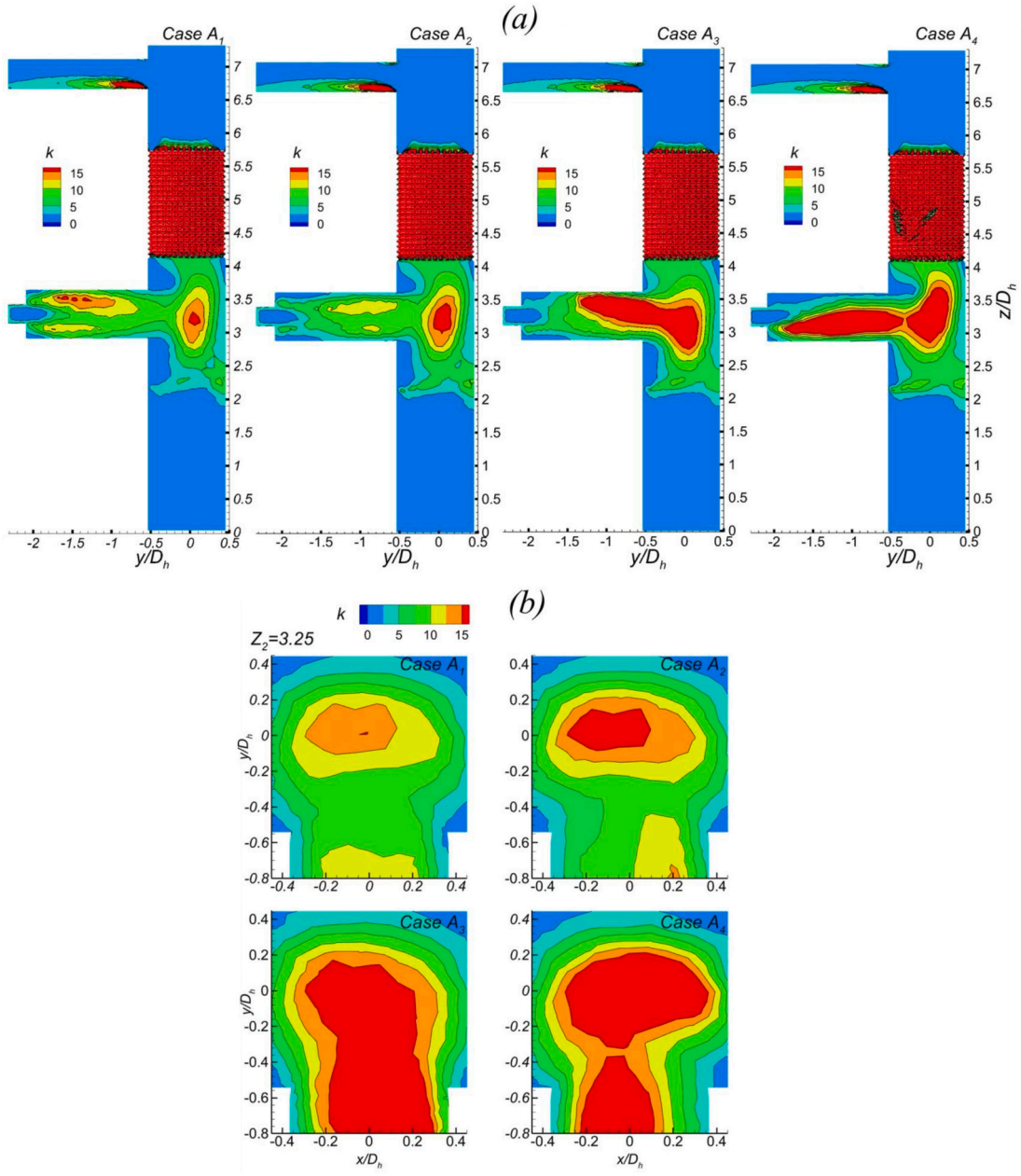


Fig. 13. TKE (k) distribution for single hot injection, Case A, (a) at the vertical y-z plane (located centrally at $x/D_h = 0$), (b) x-y plane, Z2.

This behavior explains the persistent temperature gradients observed in the cascade zone, with the highest thermal energy locked to the injection side. For configuration A, the enhancement in *k* from case A1 to A4 is clearly noticed, affirming the minor enhancement of the mixing process with an increase in injection temperature.

Dual inlet configurations (Cases B_1–B_4), by contrast, exhibit fundamentally different characteristics in both planes, as shown in Fig. 14a. At the *y-z* plane, *k* fields show two distinct, relatively higher intensity turbulence regions originating from each inlet, which rapidly merge upward to form a more expansive and centrally located turbulent core. While the *k* intensity is comparatively lower, the spread is better, *i.e.,* a uniform mixing through the entire cross section of HAS, upstream of the cascades. This behavior signals strong jet–jet interaction and crossflow-induced vortex formations, promoting enhanced thermal uniformity. At the *x-y* injection plane (Z_2), represented by Fig. 14b, it also confirms the two cores of elevated TKE zones where the two inflows intersect. The resulting turbulent core is centered and more extensive than in a single-inlet design—a signature of strong mixing that is not limited to one side but rather promotes uniform distribution of thermal and kinetic energy across the upstream system. The temperature field also demonstrates that Case B achieves better overall thermal uniformity and efficient energy transfer throughout the HAS chamber.

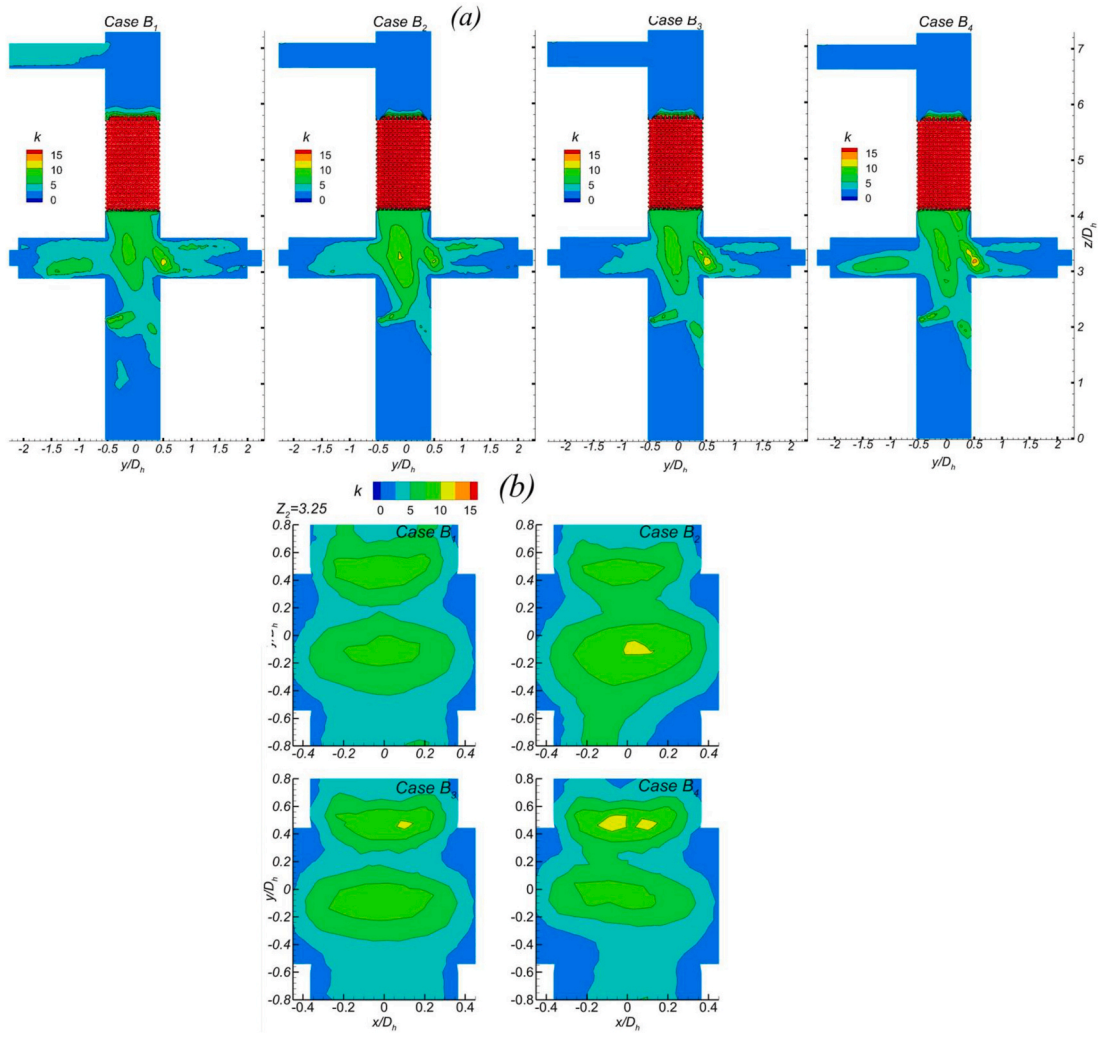


Fig. 14. TKE (k) distribution for dual hot injection, Case B, (a) at the vertical y-z plane (located centrally at $x/D_h = 0$), (b) x-y plane, Z2.

Consequently, it becomes clear that while Case A can generate effective localized mixing, it inherently lacks the symmetry and large-scale turbulence required for chamber-wide uniformity, critical for both heating efficiency and consistent aggregate drying. Case B's dual inlet system, particularly when operated at low-temperature injection (800 °C or 850 °C) and optimal mixing ratios (those that optimize jet momentum without creating excessive recirculation loss), delivers superior results by sustaining higher turbulence spread. Additionally, the lower injection temperature is likely to be beneficial in terms of energy losses and system operation. It accelerates mixing over the broader domain from the point of injection and maintains uniform temperature and velocity fields throughout the cascade region.

Summarizing the flow analysis demonstrates that the single-inlet configuration establishes an asymmetric circulation with stagnant zones that limit transport and heat redistribution. In contrast, interacting counter-jets in the dual-inlet system intensify shear production and turbulent kinetic energy and enhancing convective mixing. This flow restructuring explains the improved thermal homogenization observed in the dual-inlet cases.

4.4. Comparative analysis

To compare the outcomes of the single inlet (Case A, A1–A4) and dual inlet (Case B, B1–B4) across all studied scenarios, a comprehensive comparative analysis has been discussed in this section. The discussion has been made by highlighting the thermal performance and thermal uniformity [33], as shown in Fig. 15. Thermal performance in this context refers to the ability of the HAS configuration to provide the desired temperature to a specific region of interest (e.g., here we have selected the most important cross-sectional plane located at the center of the cascade, i.e., Z_4).

For each configuration, the mean normalized temperature ($\langle T/T_0 \rangle$) over a cross section is evaluated using the extracted data points:

$\langle \frac{T}{T_0} \rangle = \frac{1}{N} \sum_{i=1}^{N} \left(\frac{T_i}{T_0} \right)$ where T is the local temperature and T_0 is the reference (inlet) temperature, and N is the number of sampled points in that region. A higher mean normalized temperature implies better bulk heating of particles/air at that plane and thus better thermal performance. While the thermal uniformity quantifies how evenly the temperature is distributed across a selected field, high uniformity means less variation (fewer hot/cold spots). Uniformity Index is typically standard deviation (σ) and/or coefficient of variation (CV), which are calculated as: σ: $\sigma_{T/T_0} = \sqrt{\frac{1}{N} \sum_{i=1}^{N} \left(\frac{T_i}{T_0} - \langle T/T_0 \rangle \right)^2}$ and CV $= \frac{\sigma_{T/T_0}}{\langle T/T_0 \rangle}$.

Across all cases, the mean normalized temperature remains remarkably consistent, ranging from 0.490 to 0.497. This indicates that both single and dual inlet systems achieve similar levels of average heating within the cascade region, affirming that the fundamental capacity to deliver thermal energy is well maintained regardless of inlet arrangement. It's due to the effect that the total thermal energy input is the same for all cases. However, the more critical insight was observed from the uniformity indicators. Dual inlet configurations (Cases B1–B4) demonstrate notably lower standard deviations (as low as 0.080 in B1, compared to 0.117–0.132 for A1–A4) and corresponding CV (0.162 in B1, compared to up to 0.265 in A1). These metrics quantitatively show that, while the mean temperature is stable, the spatial fluctuations, i.e., hot and cold temperature zones, are significantly suppressed in the dual inlet setups, particularly for lower temperature injections.

This reduction in thermal dispersion means that the dual inlet system with low temperature injection can provide more homogeneous heating, a critical feature required for drying and recycling aggregates, where temperature uniformity is essential for consistent product quality, energy efficiency, and prevention of localized overheating or underheating. For HAS operation, this analysis conclusively highlights that while single inlets are adequate for achieving a target mean temperature, they inherently lead to higher temperature gradients and spatial non-uniformity—factors that can result in uneven material processing. By contrast, the dual inlet arrangement not only matches the average heating requirement but, more importantly, delivers smoother and more uniform thermal fields within the chamber. This makes dual inlet systems technically preferable for HAS applications demanding control over product uniformity and process reliability. However, the retrofit of dual injections indeed demands more system modification and may incur additional costs; thus, the detailed consequences of cost and retrofit difficulties will remain the scope of future work.

5. Conclusion

This study provides a detailed numerical assessment of the HAS invented for the concrete recycling unit, exploring the transition from diesel-fired to electric hot air injection. Through rigorous simulation of both single and dual inlet configurations across a realistic industrial temperature range (800–950 °C), the investigation delivers both qualitative and quantitative advancements for sustainable process design.

Quantitatively, the analysis demonstrates that the electric hot air generator achieves mean normalized cascade temperatures ($\langle T/T_0 \rangle$) in the narrow range of 0.490–0.497 for all tested cases, comparable to the heating requirement of the concrete recycling process. More importantly, the dual inlet configuration (Cases B1–B4) consistently provides superior thermal field uniformity, as evidenced by much lower standard deviations (as low as 0.080, compared to up to 0.132 in single inlet cases) and reduced coefficients of variation (CV as low as 0.162, compared to up to 0.265). For example, Case B1 achieves $\langle T/T_0 \rangle = 0.491$, $\sigma = 0.080$, and CV = 0.162, confirming highly stable and homogeneous heating across the cascade region. These metrics signify a substantial reduction in spatial temperature fluctuations and the prevalence of hot/cold spots, which are critical for process reliability and product quality. The findings are further supported by velocity and turbulent kinetic energy (TKE) field analyses, which reveal that the dual inlet system amplifies symmetric recirculation and mixing intensity—a key factor in distributing thermal energy more evenly. This configuration not only reduces localized overheating but also ensures consistent aggregate treatment, promoting energy efficiency and operational robustness.

The results indicate that successful electrification of the HAS depends primarily on inlet configuration and mixing strategy rather

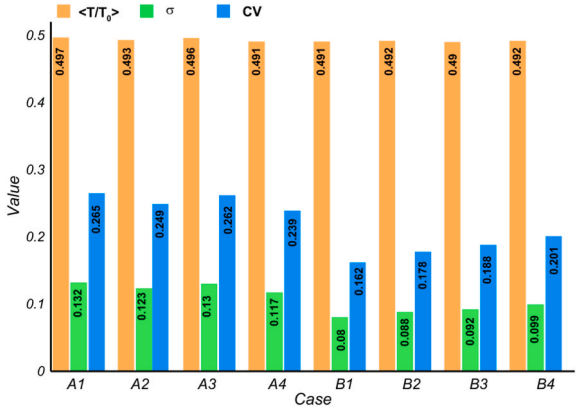


Fig. 15. Comparative analysis of thermal performance and thermal uniformity.

than on higher heating power alone. A dual symmetric injection operated at moderate temperatures (800–850 °C) provides the best balance between thermal uniformity and energy efficiency, offering a practical pathway for retrofitting existing diesel-based HAS units toward low-carbon operation. Overall, the study demonstrates that electric hot air generators in a dual-inlet arrangement represent a technically sound and operationally feasible alternative for HAS, while also providing quantitative benchmarks that support broader industrial electrification, energy savings, and cleaner production in high-temperature process applications.

CRediT authorship contribution statement

Nishab Ali: Writing – original draft, Methodology, Investigation, Formal analysis, Conceptualization. **Osama Zaid:** Writing – review & editing, Data curation. **Abraham Teklay Gebremariam:** Writing – review & editing, Supervision, Funding acquisition. **Arun Chand:** Writing – review & editing, Data curation. **Andallib Tariq:** Writing – review & editing.

Declaration of competing interest

The authors declare that they have no known competing financial interests or personal relationships that could have appeared to influence the work reported in this paper.

Acknowledgment

The authors acknowledge the financial support from the EU Horizon 2020 Project: CITADEL "Substitution of fossil Combustion in Industrial high-Temperature processes by Advanced Electrical and plasma heating technologies" (No. 101138794).

Data availability

Data will be made available on request.

References

[1] L.A. López Ruiz, X. Roca Ramón, S. Gassó Domingo, The circular economy in the construction and demolition waste sector – a review and an integrative model approach, J. Clean. Prod. 248 (2020), https://doi.org/10.1016/j.jclepro.2019.119238.
[2] A. Luciano, L. Cutaia, P. Altamura, E. Penalvo, Critical issues hindering a widespread construction and demolition waste (CDW) recycling practice in EU countries and actions to undertake: the stakeholder's perspective, Sustain. Chem. Pharm. 29 (2022), https://doi.org/10.1016/j.scp.2022.100745.
[3] European Commission, Circular economy package. http://ec.europa.eu/environment/circular-economy/index_en.htm, 2018.
[4] European Commission, GtoG Project e Gypsum to Gypsum. http://gypsumtogypsum.org/gtog-project/, 2018.
[5] C. Zhang, M. Hu, X. Yang, B. Miranda-Xicotencatl, B. Sprecher, F. Di Maio, X. Zhong, A. Tukker, Upgrading construction and demolition waste management from downcycling to recycling in the Netherlands, J. Clean. Prod. 266 (2020), https://doi.org/10.1016/j.jclepro.2020.121718.
[6] J.L. Gálvez-Martos, D. Styles, H. Schoenberger, B. Zeschmar-Lahl, Construction and demolition waste best management practice in Europe, Resour. Conserv. Recycl. 136 (2018) 166–178, https://doi.org/10.1016/j.resconrec.2018.04.016.
[7] C. Coudray, V. Amant, L. Cantegrit, A. Le Bocq, F. Thery, A. Denot, L. Eisenlohr, Influence of crushing conditions on recycled concrete aggregates (RCA) leaching behaviour, Waste Biomass Valoriz. 8 (2017) 2867–2880, https://doi.org/10.1007/s12649-017-9868-2.
[8] C.S. Poon, D. Chan, Feasible use of recycled concrete aggregates and crushed clay brick as unbound road sub-base, Constr. Build. Mater. 20 (2006) 578–585, https://doi.org/10.1016/j.conbuildmat.2005.01.045.
[9] C.S. Poon, X.C. Qiao, D. Chan, The cause and influence of self-cementing properties of fine recycled concrete aggregates on the properties of unbound sub-base, Waste Manag. 26 (2006) 1166–1172, https://doi.org/10.1016/j.wasman.2005.12.013.
[10] A. Mohammadinia, A. Arulrajah, M.M. Disfani, S. Darmawan, Small-strain behavior of cement-stabilized recycled concrete aggregate in pavement base layers, J. Mater. Civ. Eng. 31 (2019), https://doi.org/10.1061/(asce)mt.1943-5533.0002671.
[11] J.M. Allwood, Squaring the circular economy: the role of recycling within a hierarchy of material management strategies, in: Handbook of Recycling: State-Of-The-Art for Practitioners, Analysts, and Scientists, Elsevier Inc., 2014, pp. 445–477, https://doi.org/10.1016/B978-0-12-396459-5.00030-1.
[12] R. Venkatesh, C.R. Kannan, S. Manivannan, M. Vivekanandan, J.P. Krishna, A. Mezni, S. Islam, S. Rajkumar, Synthesis and experimental investigations of tribological and corrosion performance of AZ61 magnesium alloy hybrid composites, J. Nanomater. 2022 (2022), https://doi.org/10.1155/2022/6012518.
[13] R. Venkatesh, Effect of boron carbide filler on the mechanical properties of flax fiber reinforced epoxy composites, Interact 245 (2024) 1–13, https://doi.org/10.1007/s10751-024-02211-6.
[14] R. Venkatesh, Influence of silicon carbide on mechanical performance of polypropylene/hemp fiber composite for automotive applications, Interact 246 (2025), https://doi.org/10.1007/s10751-025-02251-6.
[15] A.T. Gebremariam, F. Di Maio, A. Vahidi, P. Rem, Innovative technologies for recycling end-of-life concrete waste in the built environment, Resour. Conserv. Recycl. 163 (2020), https://doi.org/10.1016/j.resconrec.2020.104911.
[16] A.T. Gebremariam, A. Vahidi, F. Di Maio, J. Moreno-Juez, I. Vegas-Ramiro, A. Łagosz, R. Mróz, P. Rem, Comprehensive study on the Most sustainable concrete design made of recycled concrete, glass and mineral wool from C& D wastes, Constr. Build. Mater. 273 (2021) 121697, https://doi.org/10.1016/j.conbuildmat.2020.121697.
[17] A. Vahidi, A. Mostaani, A. Teklay Gebremariam, F. Di Maio, P. Rem, Feasibility of utilizing recycled coarse aggregates in commercial concrete production, J. Clean. Prod. 474 (2024), https://doi.org/10.1016/j.jclepro.2024.143578.
[18] D. Ten Eycke, B.C. Johnson, The drive to electrify: benefits of electrification of fossil fuel-fired process heating equipment, in: 2024 IEEE IAS Petroleum and Chemical Industry Technical Conference (PCIC), IEEE, 2024, pp. 1–8, https://doi.org/10.1109/PCIC47799.2024.10832253.
[19] R.M. Jacob, L.-A. Tokheim, Electrified calciner concept for CO2 capture in pyro-processing of a dry process cement plant, Energy 268 (2023) 126673, https://doi.org/10.1016/j.energy.2023.126673.
[20] R.M. Jacob, J.-P. Pinheiro, L.-A. Tokheim, Electrified externally heated rotary calciner for calcination of cement raw meal, Heliyon 9 (2023) e22023, https://doi.org/10.1016/j.heliyon.2023.e22023.
[21] C. Evrim, E. Laurien, Large-eddy Simulation of turbulent thermal flow mixing in a vertical T-Junction configuration, Int. J. Therm. Sci. 150 (2020), https://doi.org/10.1016/j.ijthermalsci.2019.106231.
[22] M. Zhou, R. Kulenovic, E. Laurien, Advanced flow pattern for describing tangential flow oscillation in thermal-mixing pipe flow at a horizontal T-Junction, Int. J. Therm. Sci. 136 (2019) 328–336, https://doi.org/10.1016/j.ijthermalsci.2018.10.045.

[23] A. Maurya, N. Tiwari, R.P. Chhabra, Controlling the flow and heat transfer characteristics of power-law fluids in T-junctions using a rotating cylinder, Int. J. Therm. Sci. 163 (2021), https://doi.org/10.1016/j.ijthermalsci.2021.106854.
[24] Y. Wang, H. Li, S. Zhao, W. Chen, G. Zhou, Evaluation of fluid flow pattern and its effect on heat transfer for tube bundle in crossflow, Int. J. Therm. Sci. 218 (2025), https://doi.org/10.1016/j.ijthermalsci.2025.110169.
[25] S.B. Pope, Turbulent Flows, Cambridge University Press, 2000, https://doi.org/10.1017/CBO9780511840531.
[26] T.-H. Shih, W.W. Liou, A. Shabbir, Z. Yang, J. Zhu, A New k-ε Eddy Viscosity Model for High Reynolds Number Turbulent Flows, 1995.
[27] ANSYS, ANSYS FLUENT Theory Guide, Release 21R1, ANSYS, Inc., Canonsburg, PA, USA, pp. 1–1068.
[28] W. Zhou, H. Hu, A novel sand-dune-inspired design for improved film cooling performance, Int. J. Heat Mass Tran. 110 (2017) 908–920, https://doi.org/10.1016/j.ijheatmasstransfer.2017.03.091.
[29] N. Ali, A. Tariq, Aerothermal characteristics past a matrix structure inside a rectangular serpentine passage, Appl. Therm. Eng. 237 (2024) 121796. https://doi.org/10.1016/j.applthermaleng.2023.121796.
[30] N. Ali, A. Chand, V. Sharma, A. Tariq, Flow mechanism across 180° sharp bend of matrix-cooled serpentine channel, Int. J. Heat Fluid Flow 112 (2025). https://doi.org/10.1016/j.ijheatfluidflow.2024.109683.
[31] N. Ali, A. Tariq, Experimental study of flow physics and heat transfer across the matrix subchannels, Appl. Therm. Eng. 273 (2025) 126541. https://doi.org/10.1016/j.applthermaleng.2025.126541.
[32] A. Chand, N. Ali, A. Tariq, Experimental investigation of flow and heat transfer characteristics in the bend region of matrix channel, Exp. Therm. Fluid Sci. 172 (2026) 111632. https://doi.org/10.1016/j.expthermflusci.2025.111632.
[33] Z.U. Ahmed, Y.M. Al-Abdeli, Temperature uniformity, correlations and the flow field in swirling impinging jets, J. Therm. Sci. 32 (2023) 662–679, https://doi.org/10.1007/s11630-023-1740-z.